11

Artificial (Biomimetic) Superhydrophobic Surfaces

Abstract Artificial (biomimetic) superhydrophobic surfaces utilizing the Lotus effect are reviewed in this chapter. First, modern ways of production of superhydrophobic surfaces are discussed, including lithography, deposition, stretching, itching, evaporation, sol-gel, and others. The variety of materials used to make superhydrophobic surfaces (metals, polymers, semiconductors, nanotubes, nanoparticles) is discussed. Then wetting and self-cleaning properties of micro- and nanopatterned silicon and polymer biomimetic surfaces are presented on the basis of experimental measurements. After that, commercially available superhydrophobic products (paints, textiles, glasses) are reviewed as well as future applications in industry, bio- and nanotechnology.

In the preceding chapter, we discussed biological superhydrophobic and self-cleaning surfaces and experimental methods of their study. In this chapter, we will review artificial (biomimetic) superhydrophobic surfaces. First we will discuss various ways to produce rough superhydrophobic surfaces (Table 11.1). Second, we will review properties of these surfaces and present some applications that are coming to the market.

In recent years, fabrication of superhydrophobic surfaces has become an area of active fundamental research. This chapter will discuss a number of new approaches, and there is no doubt that in the near future new technological concepts will emerge. In general, the same techniques that are used for micro- and nanostructure manufacturing, such as lithography, etching, and deposition, have been used for producing superhydrophobic surfaces. Advantages and shortcomings of these techniques are summarized in Table 11.2. One especially interesting development is the creation of reversible surfaces that can be turned from hydrophobic to hydrophilic by applying electric potential, heat, or ultraviolet (UV) irradiation [112, 198, 207, 308, 342]. Another important task is to create transparent superhydrophobic surfaces, which may have numerous potential applications for optics and self-cleaning glasses. In order for the surface to be transparent, roughness details should be smaller than the wavelength of the visible light (about 400–700 nm) [226]. While the fundamental research is very active, a number of attempts to produce commercial products using the lotus effect have been made [118, 308]. This includes glasses, textile, paints, aerosols, etc.

Table 11.1. Typical materials and corresponding techniques to produce micro/nanoroughness [54]

Material	Technique	Contact angle	Notes	Source
Teflon	Plasma	168		Zhang et al. [354]; Shiu et al. [294]
Fluorinated block polymer solution	Casting under humid environment	160	Transparent	Yabu and Shimomura [343]
PFOS	Electro- and chemical polymerization	152	Reversible (electric potential)	Xu et al. [342]
PDMS	Laser treatment	166		Khorasani et al. [179]
PS-PDMS Block copolymer	Electrospinning	>150		Ma et al. [208]
PS, PC, PMMA	Evaporation	>150		Bormashenko et al. [58]
PS nanofiber	Nanoimprint	156		Lee et al. [203]
PET	Oxygen plasma etching	>150		Teshima et al. [314]
Organo-triethoxysilanes	Sol-gel	155	Reversible (temperature)	Shirtcliffe et al. [296]
Al	Chemical etching	>150		Qian and Shen [273]
Copper	Electrodeposition	160	Hierarchical	Shirtcliffe et al. [294]
Si	Photolithography	170		Bhushan and Jung [40]
Si	E-beam lithography	164		Martines et al. [219]
Si	X-ray lithography	>166		Fürstner et al. [118]
Si	Casting	158	Plant leaf replica	Sun et al. [308]; Fürstner et al. [118]
Si (Black Si)	Plasma etching	>150	For liquid flow	Jansen et al. [164]
Silica	Sol-gel	150		Hikita et al. (2005); Shang et al. (2005)
Polyelectrolyte multilayer surface overcoated with silica nanoparticles	Self assembly	168		Zhai et al. [352]

Table 11.1. (*Continued*)

Material	Technique	Contact angle	Notes	Source
Nano-silica spheres	Dip coating	105		Klein et al. [187]
Silica colloidal particles in PDMS	Spin coated	165	Hierarchical	Ming et al. [223]
Au clusters	Electrochemical deposition	>150		Zhang et al. [355]
Carbon nanotubes	CVD	159		Huang et al. [157]
ZnO, TiO_2 Nanorods	Sol-gel	>150	Reversible (UV irradiation)	Feng et al. [112]

11.1 How to Make a Superhydrophobic Surface

There are two main requirements for a superhydrophobic surface: the surface should be rough and it should have a hydrophobic (low surface energy) coating. These two requirements lead to two methods of producing a superhydrophobic surface. The first method is to make a rough surface from an initially hydrophobic material, and the second method is to modify an initially rough surface by changing the surface chemistry or applying a hydrophobic material. Note that roughness is usually a more critical property than low surface energy, since both moderately hydrophobic and very hydrophobic materials exhibit similar wetting behavior when roughened [207]. And understandably so, based on the simple Wenzel model, the cosine of the contact angle is given by $R_f \cos\theta_0$, so even small (negative) $\cos\theta_0$ will result in a high contact angle when combined with a big roughness factor.

Fabrication of superhydrophobic surfaces has been an area of active research since the mid-1990s. In general, the same techniques that are used for micro- and nanostructure fabrication, such as lithography, etching, and deposition, have been used to produce superhydrophobic surfaces (see Fig. 11.1).

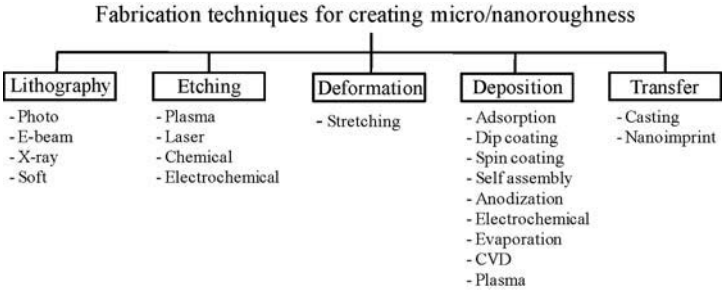

Fig. 11.1. Typical methods to fabricate micro/nanoroughening on a surface [54]

Table 11.2. Advantages and shortcomings of various fabrication techniques [54]

Techniques	Advantages	Shortcomings
Lithography	Accuracy, large area	Slow process, high cost
Etching	Fast	Chemical contamination, less control
Deposition	Flexibility, cheap	Can be high temperature, less control

11.1.1 Roughening to Create One-Level Structure

Lithography is a well-established technique for creating large areas of periodic micro/nanopatterns. It includes photo, E-beam, X-ray, and soft lithography. Bhushan and Jung [40] produced patterned Si using photolithography. To obtain a sample that is hydrophobic, a SAM of 1,1,−2,2,-tetrahydroperfluorodecyltrichlorosilane (PF_3) was deposited on the sample surfaces using the vapor phase deposition technique. They obtained a superhydrophobic surface with a contact angle up to 170°. Martines et al. [219] fabricated ordered arrays of nanopits and nanopillars by using electron beam lithography. They obtained a superhydrophobic surface with a contact angle of 164° and hysteresis of 1° for a surface consisting of tall pillars with cusped tops after a hydrophobization with octadecyltrichlorosilane (OTS). Fürstner et al. [118] created silicon wafers with regular patterns of spikes by X-ray lithography. The wafer was hydrophobized by sputtering a layer of gold and subsequent immersion in a hexadecanethiol solution. Jung and Bhushan [172] created low aspect ratio asperities (LAR, 1 : 1 height-to-diameter ratio), high aspect ratio asperities (HAR, 3 : 1 height-to-diameter ratio), and lotus pattern (replica from the lotus leaf), all on a PMMA surface using soft lithography. A self-assembled monolayer (SAM) of perfluorodecyltriethoxysilane (PFDTES) was deposited on the patterned surfaces using vapor phase deposition technique.

One well-known and effective way to make rough surfaces is etching using either plasma, laser, chemical, or electrochemical techniques [207]. Jansen et al. [164] etched a silicon wafer using a fluorine-based plasma by using the black silicon method to obtain isotropic, positively and negatively tapered as well as vertical walls with smooth surfaces. Coulson et al. [85] described an approach in plasma chemical roughening of poly(tetrafluoroethylene) (PTFE) substrates followed by the deposition of low surface energy plasma polymer layers, which give rise to high repellency toward polar and nonpolar probe liquids. A different approach was taken by Shiu et al. [294], who treated a Teflon film with oxygen plasma and obtained a superhydrophobic surface with a contact angle of 168°. Fluorinated materials have a limited solubility, which makes it difficult to roughen them. However, they may be linked or blended with other materials, which are often easier to roughen, in order to make superhydrophobic surfaces. Teshima et al. [314] obtained a transparent superhydrophobic surface from a poly(ethylene terephthalate) (PET) substrate via selective oxygen plasma etching followed by plasma-enhanced chemical vapor deposition using tetramethylsilane (TMS) as the precursor. Khorasani et al. [179] produced

porous PDMS surfaces with a contact angle of 175° using a CO_2-pulsed laser etching method as an excitation source for the surface. Qian and Shen [273] described a simple surface roughening method by dislocation selective chemical etching on polycrystalline metals such as aluminum. After treatment with fluoroalkylsilane, the etched metallic surfaces exhibited superhydrophobicity. Xu et al. [342] fabricated a reversible superhydrophobic surface with a double-roughened perfluorooctanesulfonate (PFOS) doped conducting polypyrrole (PPy) film by a combination of electropolymerization and chemical polymerization. The reversibility was achieved by switching between superhydrophobic doped or oxidized states and superhydrophilicity dedoped or neutral states with changing the applied electrochemical potential.

The stretching method can be used to produce a superhydrophobic surface. Zhang et al. [354] stretched a Teflon film and converted it into fibrous crystals with a large fraction of void space in the surface, leading to high roughness and superhydrophobicity.

Deposition methods also make a substrate rough from the bulk properties of the material and enlarge potential applications of superhydrophobic surfaces. There are several ways to make a rough surface including adsorption, dip coating, electrospinning, anodization, electrochemical, evaporation, chemical vapor deposition (CVD), and plasma. Solidification of wax can be used to produce a superhydrophobic surface. Shibuichi et al. [293] used alkylketene dimer (AKD) wax on a glass plate to spontaneously form a fractal structure in its surfaces. They obtained a surface with a contact angle larger than 170° without any fluorination treatments. Klein et al. [187] obtained superhydrophobic surfaces by simply dip-coating a substrate with slurry containing nano-silica spheres, which adhered to a substrate after a low temperature heat treatment. After reaction of the surface with a fluoroalkyltrichlorosilane, the hydrophobicity increased with decreasing area fraction of spheres. Ma et al. [208, 209] produced block copolymer poly(styrene-b-dimethylsiloxane) fibers with submicrometer diameters in the range 150–400 nm by electrospinning from solution in tetrahydrofuran and dimethylformamide. They obtained superhydrophobic nonwoven fibrous mats with a contact angle of 163°. Shiu et al. [294] showed that self-organized, close-packed superhydrophobic surfaces can be easily achieved by spin-coating the monodispersed polystyrene beads solution on substrate surfaces. The sizes of the beads were reduced by controlling the etching conditions. After plasma treatment, the surfaces were coated with a layer of gold and eventually a layer of octadecanethiol SAM to render hydrophobicity. Abdelsalam et al. [1] studied the wetting of structured gold surfaces formed by electrodeposition through a template of submicrometer spheres and discussed the role of the pore size and shape in controlling wetting. Bormashenko et al. [58] used evaporated polymer solutions of polystyrene (PS), polycarbonate (PC), and polymethylmethacrylate (PMMA) dissolved in chlorinated solvents, dichloromethane (CH_2Cl_2), and chloroform ($CHCl_3$), to obtain a self-assembled structure with hydrophobic properties. Chemical/physical vapor deposition (CVD/PVD) has been used to modify surface chemistry as well. Lau et al. [201] created superhydrophobic carbon nanotube forests by modifying the surface of vertically aligned nanotubes with plasma enhanced chemical vapor deposition (PECVD). Superhydrophobicity was achieved down to the microscopic level

where essentially spherical, micrometer-sized water droplets can be suspended on top of the nanotube forest. Zhu et al. [360] and Huang et al. [157] prepared surfaces with two-scale roughness by controlled growth of carbon nanotube (CNT) arrays by CVD. Zhao et al. [358] also synthesized the vertically aligned multiwalled carbon nanotube (MWCNT) arrays by chemical-vapor deposition on Si substrates using thin film of iron (Fe) as catalyst layer and aluminum (Al) film.

Attempts to create a superhydrophobic surface by casting and nanoimprint methods have been successful. Yabu and Shimomura [343] prepared a porous superhydrophobic transparent membrane by casting a fluorinated block polymer solution in a humid environment. The transparency was achieved because the honeycomb-patterned films had subwavelength pore size. Sun et al. [308] reported a nanocasting method to make a superhydrophobic PDMS surface. They first made a negative PDMS template using the lotus leaf as an original template and then used the negative template to make a positive PDMS template—a replica of the original lotus leaf. Zhao et al. [358] prepared a superhydrophobic surface by casting a micellar solution of a copolymer poly(styrene-b-dimethylsiloxane) (PS-PDMS) in humid air based on the cooperation of vapor-induced phase separation and surface enrichment of PDMS block. Lee et al. [203] produced vertically aligned PS nanofibers by using nanoporous anodic aluminum oxide as a replication template in a heat- and pressure-driven nanoimprint pattern transfer process. As the aspect ratio of the polystyrene (PS) nanofibers increased, the nanofibers could not stand upright but formed twisted bundles resulting in a three-dimensionally rough surface with advancing and receding contact angles of 155.8° and 147.6°, respectively.

11.1.2 Coating to Create One-Level Hydrophobic Structures

Modifying the surface chemistry with a hydrophobic coating widens the potential applications of superhydrophobic surfaces. There are several ways to modify the chemistry of a surface, including sol-gel, dip coating, self-assembly, electrochemical, and chemical/physical vapor deposition. Shirtcliffe et al. [296] prepared porous sol-gel foams from organo-triethoxysilanes which exhibited switching between superhydrophobicity and superhydrophilicity when exposed to different temperatures. The critical switching temperature was between 275 °C and 550 °C for different materials, and when the foam was heated above the critical temperature, complete rejection of water by the cavities switched to complete filling of the pores. Hikita et al. [152] used colloidal silica particles and fluoroalkylsilane as the starting materials and prepared a sol-gel film with superliquid-repellency by hydrolysis and condensation of alkoxysilane compounds. Feng et al. [112] produced superhydrophobic surfaces using ZnO nanorods by sol-gel method. They showed that superhydrophobic surfaces can be switched into hydrophilic surfaces by alternation of ultraviolet (UV) irradiation. Shang et al. [290] did not blend low surface energy materials in the sols, but described a procedure to make transparent superhydrophobic surfaces by modifying silica-based gel films with a fluorinated silane. In a similar way, Wu et al. [341] made a microstructured ZnO-based surface via a wet chemical process

and obtained superhydrophobicity after coating the surface with long-chain alkanoic acids.

Zhai et al. [352] used a layer-by-layer (LBL) self-assembly technique to create a poly(allylamine hydrochloride)/poly(acrylic acid) (PAH/PAA) multilayer which formed a honeycomb-like structure on the surface after an appropriate combination of acidic treatments. After cross-linking the structure, they deposited silica nanoparticles on the surface via alternating dipping of the substrates into an aqueous suspension of the negatively charged nanoparticles and an aqueous PAH solution, followed by a final dipping into the nanoparticle suspension. Superhydrophobicity was obtained after the surface was modified by a chemical vapor deposition of (tridecafluoro-1,1,2,2-tetrahydrooctyl)-1-trichlorosilane followed by a thermal annealing.

Zhang et al. [355] showed that the surface covered with dendritic gold clusters, which was formed by electrochemical deposition onto indium tin oxide (ITO) electrode modified with a polyelectrolyte multilayer, showed superhydrophobic properties after further deposition of an *n*-dodecanethiol monolayer. Han et al. [142] described the fabrication of lotus leaf-like superhydrophobic metal surfaces by using electrochemical reaction of Cu or Cu–Sn alloy plated on steel sheets with sulfur gas, and subsequent perfluorosilane treatment. The chemical bath deposition (CBD) has also been used to make nanostructured surfaces, thus, Hosono et al. [155] fabricated a nanopin film of brucite-type cobalt hydroxide (BCH) and achieved a contact angle of 178° after further modification with lauric acid (LA). Shi et al. [292] described the use of galvanic cell reaction as a facile method to chemically deposit Ag nanostructures on the *p*-silicon wafer on a large scale. When the Ag covered silicon wafer was further modified with a self-assembled monolayer of *n*-dodecanethiol, a superhydrophobic surface was obtained with a contact angle of about 154° and a tilt angle lower than 5°.

11.1.3 Methods to Create Two-Level (Hierarchical) Superhydrophobic Structures

Two-level (hierarchical) roughness structures are typical for superhydrophobic surfaces in nature, as we discussed earlier. Recently, much effort has been devoted to fabricating these hierarchical structures in various ways. Shirtcliffe et al. [294] prepared a hierarchical (double-roughened) copper surface by electrodeposition from acidic copper sulfate solution onto flat copper and patterning technique of coating with a fluorocarbon hydrophobic layer. Another way to obtain a rough surface for superhydrophobicity is assembly from colloidal systems. Ming et al. [223] prepared a hierarchical (double roughened) surface consisting of silica-based raspberry-like particles which were made by covalently grafting amine-functionalized silica particles of 70 nm to epoxy-functionalized silica particles of 700 nm via the reaction between epoxy and amine groups. The surface became superhydrophobic after being modified with PDMS. Northen and Turner [231] fabricated arrays of flexible silicon dioxide platforms supported by single high aspect ratio silicon pillars down to 1 μm in diameter and with heights up to ∼50 μm. When these platforms were coated

with polymeric organorods approximately 2 μm tall and 50–200 nm in diameter, it showed that the surface is highly hydrophobic with a water contact angle of 145°. Chong et al. [81] used the combination of the porous anodic alumina (PAA) template with microsphere monolayers to fabricate hierarchically ordered nanowire arrays, which have periodic voids at the microscale and hexagonally packed nanowires at the nanoscale. They created the arrays by selective electrodeposition using nanoporous anodic alumina as a template and a porous gold film as a working electrode that is patterned by microsphere monolayers. Wang et al. [333] also developed a novel precursor hydrothermal redox method with $Ni(OH)_2$ as the precursor to fabricate a hierarchical structure of nickel hollow microspheres with nickel nanoparticles as the in situ formed building units. Wang et al.'s hierarchical hollow structure exhibited enhanced coercivity and remnant magnetization as compared with hollow nickel submicrometer spheres, hollow nickel nanospheres, bulk nickel, and free Ni nanoparticles. Kim et al. [185] fabricated a hierarchical structure that looks like the same structure as a lotus leaf. First, nanoscale porosity was generated by anodic aluminum oxidation, then the anodized porous alumina surface was replicated by polytetrafluoroethylene. The polymer sticking phenomenon during the replication created the submicrostructures on the negative polytetrafluoroethylene nanostructure replica. The contact angle of the created hierarchical structure was obtained about 160° and the tilting angle is less than 1°. Del Campo and Greiner [95] reported that SU-8 hierarchical patterns composed of features with lateral dimensions ranging from 5 mm to 2 mm and heights from 10 to 500 μm were obtained by photolithography which comprises a step of layer-by-layer exposure in soft contact printed shadow masks which are embedded into the SU-8 multilayer.

11.2 Experimental Techniques

11.2.1 Contact Angle, Surface Roughness, and Adhesion

The static and dynamic (advancing and receding) contact angles were measured using a Rame–Hart model 100 contact angle goniometer and water droplets of deionized water [39, 68, 172]. For the measurement of static contact angle, the droplet size should be small but larger than the dimension of the structures present on the surfaces. Droplets of about 5 μL in volume (with a diameter of a spherical droplet about 2.1 mm) were gently deposited on the substrate using a microsyringe for the static contact angle. The receding contact angle was measured by the removal of water from a DI water sessile droplet (~5 μL) using a microsyringe. The advancing contact angle was measured by adding additional water to the sessile droplet (~5 μL) using the microsyringe. The contact angle hysteresis was calculated by the difference between the measured advancing and receding contact angles. The tilt angle was measured by a simple stage-tilting experiment with the droplets of 5 μL volume [40, 41]. All measurements were made using five different points for each sample at 22 ± 1 °C and 50 ± 5% RH. The measurements were reproducible to with ±3%.

For surface roughness, an optical profiler (NT-3300, Wyko Corp., Tucson, AZ) was used for different surface structures [39–41, 53, 68, 174]. A greater Z-range

of the optical profiler of 2 mm is a distinct advantage over the surface roughness measurements using an AFM which has a Z-range of 7 μm, but it has a maximum lateral resolution of approximately 0.6 μm [31, 32]. Experiments were performed using three different radii tips to study the effect of scale dependence. Large radii atomic force microscopy (AFM) tips were primarily used in this study. Borosilicate ball with 15 μm and a silica ball with 3.8 μm radius were mounted on a gold-coated triangular Si_3N_4 cantilever with a nominal spring constant of $0.58\,N\,m^{-1}$. A square pyramidal Si_3N_4 tip with a nominal radius 30–50 nm on a triangular Si_3N_4 cantilever with a nominal spring constant of $0.58\,N\,m^{-1}$ was used for smaller radius tip. Adhesive force was measured using the single point measurement of a force calibration plot [31, 32, 34].

11.2.2 Measurement of Droplet Evaporation

Droplet evaporation was observed and recorded by a digital camcorder (Sony, DCRSR100) with a 10 X optical and 120 X digital zoom for every run of the experiment. Then the decrease in the diameter of the droplets with time was determined [173, 174]. Time resolution of the camcorder was 0.03 s per frame. An objective lens placed in front of the camcorder during recording gave a total magnification of between 10 to 20 times. Droplet diameters as small as a few hundred microns could be measured with this method. Droplets were gently deposited on the substrate using a microsyringe, and the whole process of evaporation was recorded. The evaporation starts right after the deposition of the droplets. Images obtained were analyzed using Imagetool® software (University of Texas Health Science Center) for the contact angle. To find the dust trace remaining after droplet evaporation, an optical microscopy with a CCD camera (Nikon, Optihot-2) was used. All measurements were made in a controlled environment at $22 \pm 1\,^{\circ}C$ and $45 \pm 5\%$ RH [173, 174].

11.2.3 Measurement of Contact Angle Using ESEM

A Philips XL30 ESEM equipped with a Peltier cooling stage was used to study smaller droplets [174]. ESEM uses a gaseous secondary electron detector (GSED) for imaging. The SESM column is equipped with a multistage differential pressure-pumping unit. The pressure in the upper part is about 10^{-6} to 10^{-7} Torr, but the pressure of about 1 to 15 Torr can be maintained in the observation chamber. When the electron beam (primary electrons) ejects secondary electrons from the surface of the sample, the secondary electrons collide with gas molecules in the ESEM chamber, which in turn acts as a cascade amplifier, delivering the secondary electron signal to the positively biased GSED. The positively charged ions are attracted toward the specimen to neutralize the negative charge produced by the electron beam. Therefore, the ESEM can be used to examine electrically isolated specimens in their natural state. In ESEM, adjusting the pressure of the water vapor in the specimen chamber and the temperature of the cooling stage will allow the water to condense on the sample in the chamber. For the measurement of the static and dynamic contact angles on patterned surfaces, the video images were recorded. The voltage of the electron

beam was 15 kV and the distance of the specimen from the final aperture was about 8 mm. If the angle of observation is not parallel to the surface, the electron beam is not parallel to the surface but inclined at an angle, this will produce a distortion in the projection of the droplet profile. A mathematical model to calculate the real contact angle from the ESEM images was used to correct the tilting of the surfaces during imaging [65, 174].

11.3 Wetting of Micro- and Nanopatterned Surfaces

In this section, we will discuss experimental observations of wetting properties of micro- and nanopatterned surfaces on the basis of the experimental data by Jung and Bhushan [173] and other groups.

11.3.1 Micro- and Nanopatterned Polymers

Jung and Bhushan [172] studied two types of polymers: poly(methyl methacrylate) (PMMA) and polystyrene (PS). PMMA and PS were chosen because they are widely used in MEMS/NEMS devices. Both hydrophilic and hydrophobic surfaces can be produced using these two polymers, as PMMA has polar groups with high surface energy (hydrophilic) while PS has electrically neutral and nonpolar groups (hydrophobic) with low surface energy. Furthermore, a PMMA structure can be made hydrophobic by treating it appropriately, for example, by coating with a hydrophobic self-assembled monolayer (SAM).

Four types of surface patterns were fabricated from PMMA: a flat film, low aspect ratio asperities (LAR, 1 : 1 height-to-diameter ratio), high aspect ratio asperities (HAR, 3 : 1 height-to-diameter ratio), and the lotus pattern (replica of the lotus leaf). Two types of surface patterns were fabricated from PS: a flat film and the lotus pattern. Figure 11.2 shows SEM images of the two types of nanopatterned structures, LAR and HAR, and the one type of micropatterned structure, lotus pattern, all on a PMMA surface [67, 172]. For nanopatterned structures, PMMA film was spin-coated on the silicon wafer. A UV cured mold (PUA mold) with nanopatterns of interest was made which enables one to create sub-100-nm patterns with high aspect ratio [80]. The mold was placed on the PMMA film and a slight pressure of $\sim$10 g/cm^2 ($\sim$1 kPa) was applied and annealed at 120 °C. Finally, the PUA mold was removed from PMMA film. For micropatterned structures, a polydimethylsiloxane (PDMS) mold was first made by casting PDMS against a lotus leaf followed by heating. As shown in Fig. 11.2, it can be seen that only microstructures exist on the surface of lotus pattern [172].

Since PMMA by itself is hydrophilic, in order to obtain a hydrophobic sample, a self-assembled monolayer (SAM) of perfluorodecyltriethoxysilane (PFDTES) was deposited on the sample surfaces using vapor phase deposition technique. PFDTES was chosen because of its hydrophobic nature. The deposition of PFDTES took place at a temperature of 100 °C, pressure 400 atm, with 20 min deposition time, and 20 min annealing time. The polymer surface was exposed to an oxygen plasma

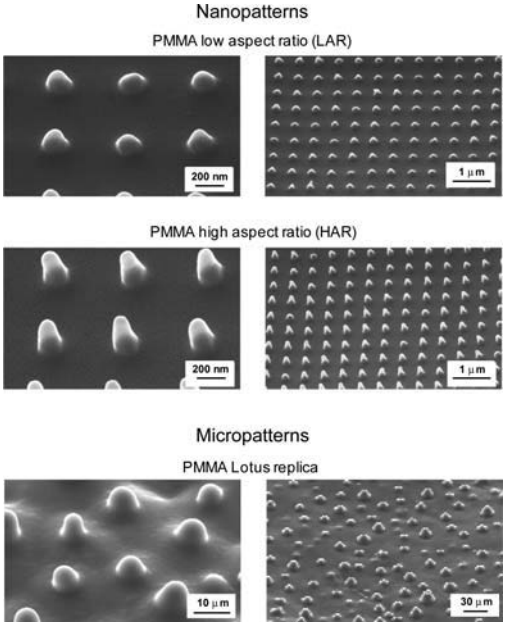

Fig. 11.2. Scanning electron micrographs of the two nanopatterned polymer surfaces (shown using two magnifications to see both the asperity shape and the asperity pattern on the surface) and the micropatterned polymer surface (lotus pattern, which has only microstructures on the surface) [67, 172]

treatment (40 W, O_2 187 Torr, 10 s) prior to coating. The oxygen plasma treatment is necessary to oxidize any organic contaminants on the polymer surface and to also alter the surface chemistry to allow for enhanced bonding between the SAM and the polymer surface [172].

11.3.1.1 Contact Angle Measurements

Jung and Bhushan [172] measured the static contact angle of water with the patterned PMMA and PS structures; see Fig. 11.3. Since the Wenzel roughness factor is the parameter that often determines wetting behavior, we calculated the roughness factor and it is presented in Table 11.3 for various samples. The data show that the contact angle of the hydrophilic materials decreases with an increase in the roughness factor, as predicted by the Wenzel model. When the polymers were coated with PFDTES, the film surface became hydrophobic. Figure 11.3 also shows the contact angle for various PMMA samples coated with PFDTES. For a hydrophobic surface, the standard Wenzel model predicts an increase of contact angle with roughness factor, which is what happens in the case of patterned samples. We also present the calculated values of the contact angle for various patterned samples based on the contact angle of the smooth film and the Wenzel equa-

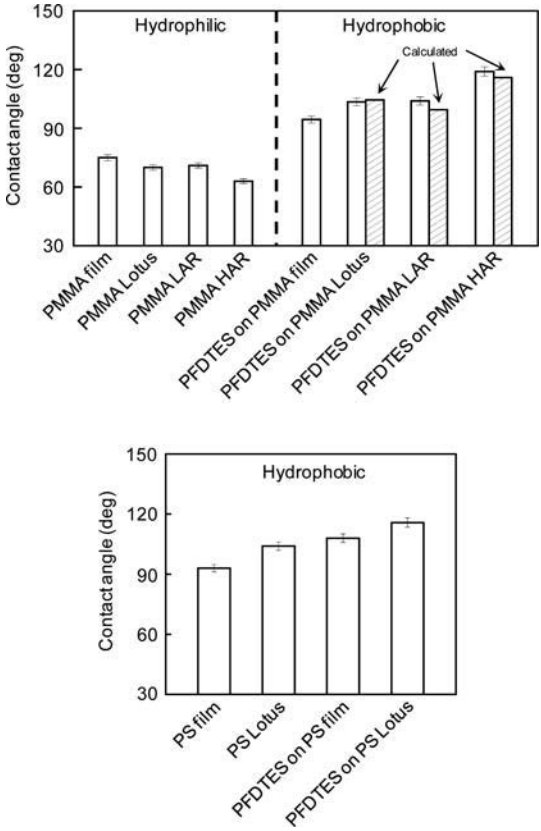

Fig. 11.3. Contact angles for various patterned surfaces on PMMA and PS polymers [172]

Table 11.3. Roughness factor for micro- and nanopatterned polymers [172]

	LAR	HAR	Lotus
R_f	2.1	5.6	3.2

tion. The measured contact angle values for the lotus pattern were comparable with the calculated values, whereas for the LAR and HAR patterns they are higher. It suggests that nanopatterns benefit from air pocket formation. For the PS material, the contact angle of the lotus pattern also increased with increased roughness factor.

11.3.1.2 Scale Dependence on Adhesive Force

Jung and Bhushan [172] found that scale-dependence of adhesion and friction are important for this study because the tip/surface interface area changes with size. The meniscus force will change due to either changing tip radius, the hydrophobicity of

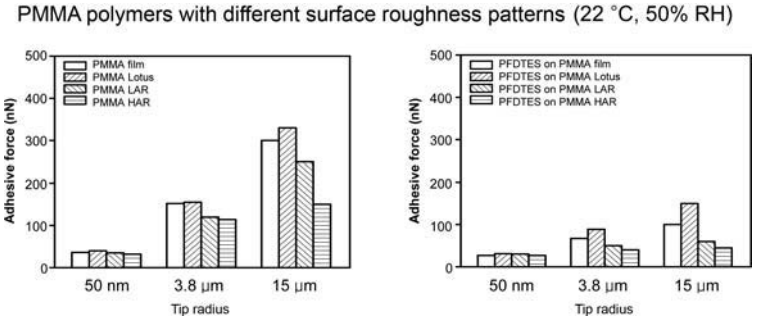

Fig. 11.4. Scale dependent adhesive force for various patterned surfaces measured using AFM tips of various radii [172]

the sample, or the number of contact and near-contacting points. Figure 11.4 shows the dependence of the tip radius and hydrophobicity on the adhesive force for PMMA and PFDTES coated on PMMA [172]. When the radius of the tip is changed, the contact angle of the sample is changed, and asperities are added to the sample surface, the adhesive force will change due to the change in the meniscus force and the real area of contact.

The two plots in Fig. 11.4 show the adhesive force on a linear scale for the different surfaces with varying tip radius. The left bar chart in Fig. 11.4 is for hydrophilic PMMA film, lotus pattern, LAR, and HAR, and shows the effect of tip radius and hydrophobicity on adhesive force. For increasing radius, the adhesive force increases for each material. With a larger radius, the real area of contact and the meniscus contribution increase, resulting in increased adhesion. The right bar chart in Fig. 11.4 shows the results for PFDTES coated on each material. These samples show the same trends as the film samples, but the increase in adhesion is not as dramatic. The hydrophobicity of PFDTES on material reduces meniscus forces, which in turn reduces adhesion from the surface. The dominant mechanism for the hydrophobic material is real area of contact and not meniscus force, whereas with hydrophilic material there is a combination of real area of contact and meniscus forces [172].

11.3.2 Micropatterned Si Surfaces

Micropatterned surfaces produced from single-crystal silicon (Si) by electrolithography and coated with a self-assembled monolayer (SAM) were used in the study by Jung and Bhushan [173, 174]. Silicon has traditionally been the most commonly used structural material for micro/nanocomponents. A Si surface can be made hydrophobic by coating with a SAM. One purpose of this investigation was to study the transition for Cassie–Baxter to Wenzel regimes by changing the distance between the pillars. To create patterned Si, two series of nine samples each were fabricated using photolithography [22]. Series 1 has 5-µm diameter and 10-µm height flat-top, cylindrical pillars with different pitch values (7, 7.5, 10, 12.5, 25, 37.5, 45, 60, and 75) µm, and Series 2 has 14-µm diameter and 30-µm height flat-top, cylindrical pillars with

different pitch values (21, 23, 26, 35, 70, 105, 126, 168, and 210) μm. The pitch is the spacing between the centers of two adjacent pillars. The Si chosen were initially hydrophilic, so to obtain a sample that is hydrophobic, a self-assembled monolayer (SAM) of 1,1,−2,2,-tetrahydroperfluorodecyltrichlorosilane (PF_3) was deposited on the sample surfaces using the vapor phase deposition technique [22]. PF_3 was chosen because of the hydrophobic nature of the surface. The thickness and rms roughness of the SAM of PF_3 were 1.8 nm and 0.14 nm, respectively [176].

An optical profiler was used to measure the surface topography of the patterned surfaces [40, 53, 173]. One sample each from the two series was chosen to characterize the surfaces. Two different surface height maps can be seen for the patterned Si in Fig. 11.5. In each case, a 3D map and a flat map along with a 2D profile in a given location of the flat 3D map are shown. A scan size of 100 μm × 90 μm was used to obtain a sufficient number of pillars to characterize the surface but also to maintain enough resolution to get an accurate measurement.

The images found with the optical profiler indicate that the flat-top, cylindrical pillars on the Si surface are distributed on the entire surface. These pillars were distributed in a square grid with different pitch values. Each sample series has the same series of Wenzel roughness factors ($R_f = 1 + \pi DH/P^2$) and other relevant geometric parameters (e.g., the spacing factor $S_f = P/H$). Keeping these parameters constant means that Cassie and Baxter's and Wenzel's theoretical models predict exactly the same series of contact angle values for all two series of nine samples [173].

11.3.2.1 Contact Angle for Flat-Top, Cylindrical Pillars

Let us consider the geometry of flat-top, cylindrical pillars of diameter D, height H, and pitch P, distributed in a regular square array as shown in Fig. 11.5. For the special case of the droplet size much larger than P (of interest in this study), a droplet contacts the flat-top of the pillars forming the composite interface, and the cavities are filled with air. For this case,

$$f_{LA} = 1 - \frac{\pi D^2}{4P^2} = 1 - f_{SL}$$

and the contact angles for the Wenzel and Cassie–Baxter regimes are given by corresponding equations.

Geometrical values of the flat-top, cylindrical pillars in series 1 and 2 are used for calculating the contact angle for the above-mentioned two cases. Figure 11.6 shows the plot of the predicted values of the contact angle as a function of pitch between the pillars for the two cases. Wenzel's and Cassie and Baxter's equations present two possible equilibrium states for a water droplet on the surface. This indicates that there is a critical pitch below which the composite interface dominates and above which the homogeneous interface dominates the wetting behavior. The process to design superhydrophobic surfaces is important in determining the equilibrium water droplet. Therefore, one needs to find the critical point that can be used to design superhydrophobic surfaces. It should also be noted that even in cases where the liquid droplet does not contact the bottom of the cavities, the water droplet in a metastable

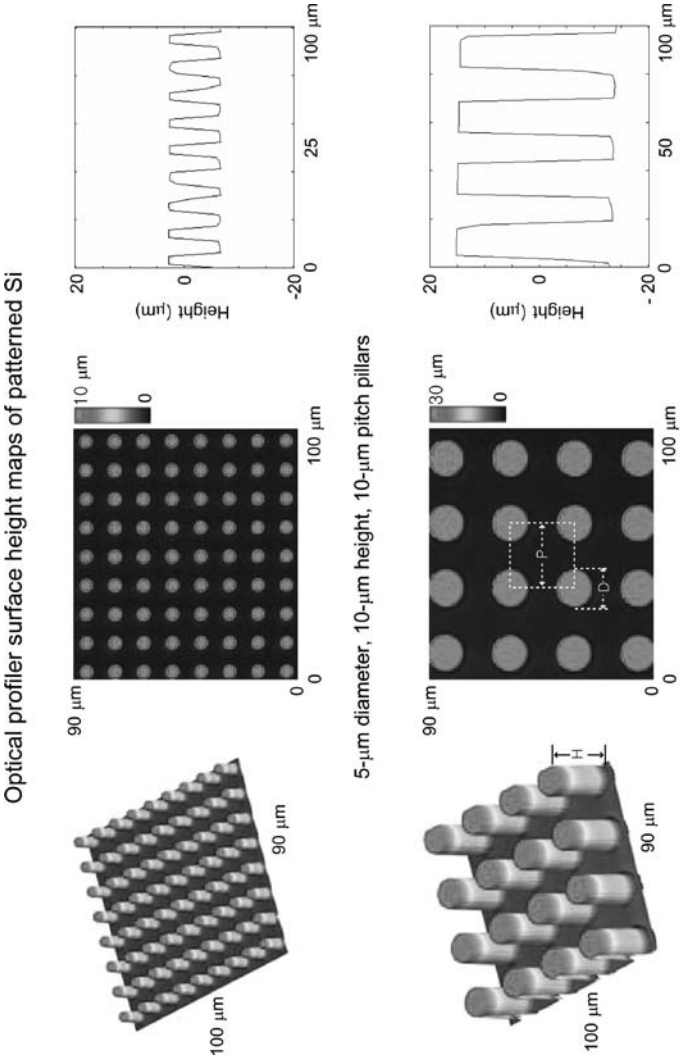

Fig. 11.5. Surface height maps and 2-D profiles of the patterned surfaces using an optical profiler [40]

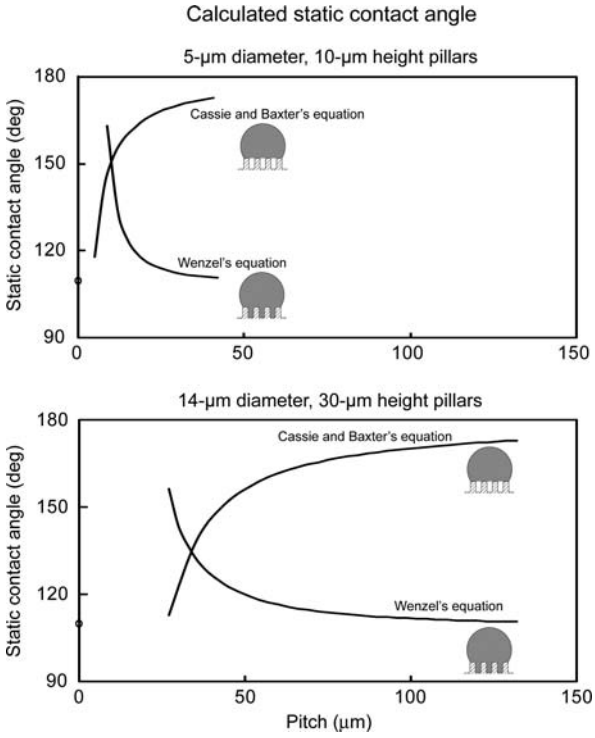

Fig. 11.6. Calculated static contact angle as a function of geometric parameters for a given value of θ_0 using Wenzel and Cassie and Baxter equations for two series of the patterned surfaces with different pitch values [40]

state becomes unstable and transition from the Cassie–Baxter regime to the Wenzel regime occurs if the pitch is large.

11.3.2.2 Curvature-Based Cassie–Wenzel Transition Criteria

A stable composite interface is essential for the successful design of superhydrophobic surfaces. However, the composite interface is fragile, and it may transform into the homogeneous interface. What triggers the transition between the regimes remains a subject of debate, although a number of explanations have been suggested. Nosonovsky and Bhushan [243] studied destabilizing factors for the composite interface and found that a convex surface (with bumps) leads to a stable interface and high contact angle. Also, they suggested that a droplet's weight and curvature are among the factors which affect the transition.

Bhushan and Jung [40, 41] and Jung and Bhushan [173, 174] investigated the effect of droplet curvature on the Cassie–Wenzel regime transition. First, they considered a small water droplet suspended on a superhydrophobic surface consisting of a regular array of circular pillars with diameter D, height H, and pitch P as shown

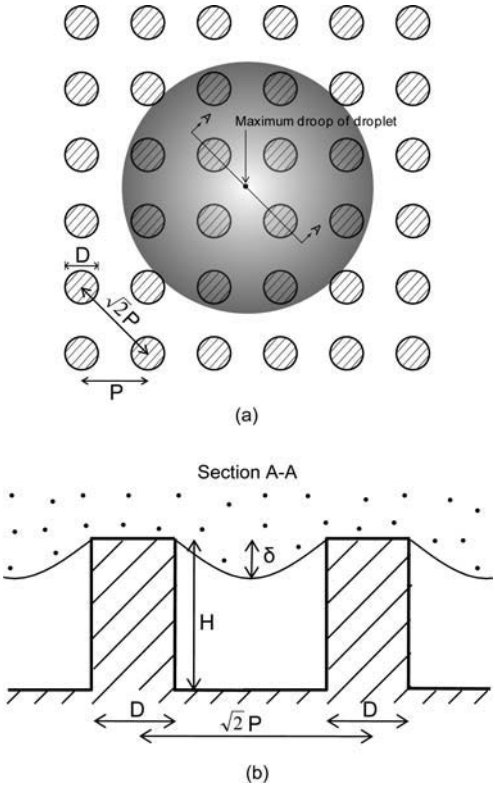

Fig. 11.7. A small water droplet suspended on a superhydrophobic surface consisting of a regular array of circular pillars. **a** Plan view. The maximum droop of droplet occurs in the center of square formed by four pillars. **b** Side view in section A-A. The maximum droop of droplet (δ) can be found in the middle of two pillars which are diagonally across [173, 174]

in Fig. 11.7. The local deformation for small droplets is governed by surface effects rather than gravity. The curvature of a droplet is governed by the Laplace equation, which relates the pressure inside the droplet to its curvature [6]. Therefore, the curvature is the same at the top and at the bottom of the droplet [197, 244]. For the patterned surface considered here, the maximum droop of the droplet occurs in the center of the square formed by the four pillars as shown in Fig. 11.7(a). Therefore, the maximum droop of the droplet, δ, in the recessed region can be found in the middle of two pillars which are diagonally across as shown in Fig. 11.7(b), which is $(\sqrt{2}P - D)^2/(8R)$. If the droop is much greater than the depth of the cavity

$$\left(\sqrt{2}P - D\right)^2/R \geq H, \tag{11.1}$$

then the droplet will just contact the bottom of the cavities between pillars, resulting in the transition from the Cassie–Baxter to Wenzel regime. Furthermore, in the case of large distances between the pillars, the liquid–air interface can easily be destabilized due to dynamic effects, such as surface waves that are formed at the liquid–air

interface due to the gravitational or capillary forces. This leads to the formation of the homogeneous solid–liquid interface. However, whether the droplet droop or other mechanisms dominate the transition remains to be investigated, as we discussed in Sect. 8.2.

11.3.2.3 Contact Angle Measurements

The experiment performed with 1 mm in radius (5 μL volume) droplets on the patterned Si coated with PF_3 was designed to determine the static contact angle [40, 41, 173, 174]. The contact angles on the prepared surfaces are plotted as a function of pitch between the pillars in Fig. 11.8(a). A dotted line represents the transition criteria range obtained using (11.1). The flat Si coated with PF_3 showed a static contact angle of 109°. As the pitch increases up to 45 μm of series 1 and 126 μm of series 2, the static contact angle first increases gradually from 152° to 170°. Then, the contact angle starts decreasing sharply. Initial increase with an increase of pitch has to do with more open air space present which increases the propensity of air pocket formation. As predicted from the Jung and Bhushan [173] transition criteria (11.1), the decrease in contact angle at higher pitch values results due to the transition from composite interface to solid–liquid interface. In series 1, the value predicted from the transition criteria is a little higher than the experimental observations. However, in series 2, there is a good agreement between the experimental data and the theoretically predicted values by Jung and Bhushan [173] for the transition from Cassie and Baxter regime to Wenzel regime.

Figure 11.8(b) shows hysteresis and tilt angle as a function of pitch between the pillars [40, 41]. The flat Si coated with PF_3 showed a hysteresis angle of 34° and tilt angle of 37°. The patterned surfaces with low pitch increase the hysteresis and tilt angles compared to the flat surface due to the effect of sharp edges on the pillars, resulting in pinning [240]. Hysteresis for a flat surface can arise from roughness and surface heterogeneity. For a droplet moving down the inclined patterned surfaces, the line of contact of the solid, liquid, and air will be pinned at the edge point until it is able to move, resulting in increasing hysteresis and tilt angles. Figure 11.9 shows droplets on patterned Si with 5-μm diameter and 10-μm height pillars with different pitch values. The asymmetrical shape of the droplet signifies pinning. The pinning on the patterned surfaces can be observed as compared to the flat surface. The patterned surface with low pitch (7 μm) has more pinning than the patterned surface with high pitch (37.5 μm), because the patterned surface with low pitch has more sharp edges contacting with a droplet.

For various pitch values, hysteresis and tilt angles show the same trends with varying pitch between the pillars. After an initial increase as discussed earlier, they gradually decrease with increasing pitch (due to reduced number of sharp edges) and show an abrupt minimum in the value which has the highest contact angle. The lowest hysteresis and tilt angles are 5° and 3°, respectively, which were observed on the patterned Si with 45 μm of series 1 and 126 μm of series 2. As discussed earlier, an increase in the pitch value allows the formation of composite interface. At higher pitch values, it is difficult to form the composite interface. The decrease in

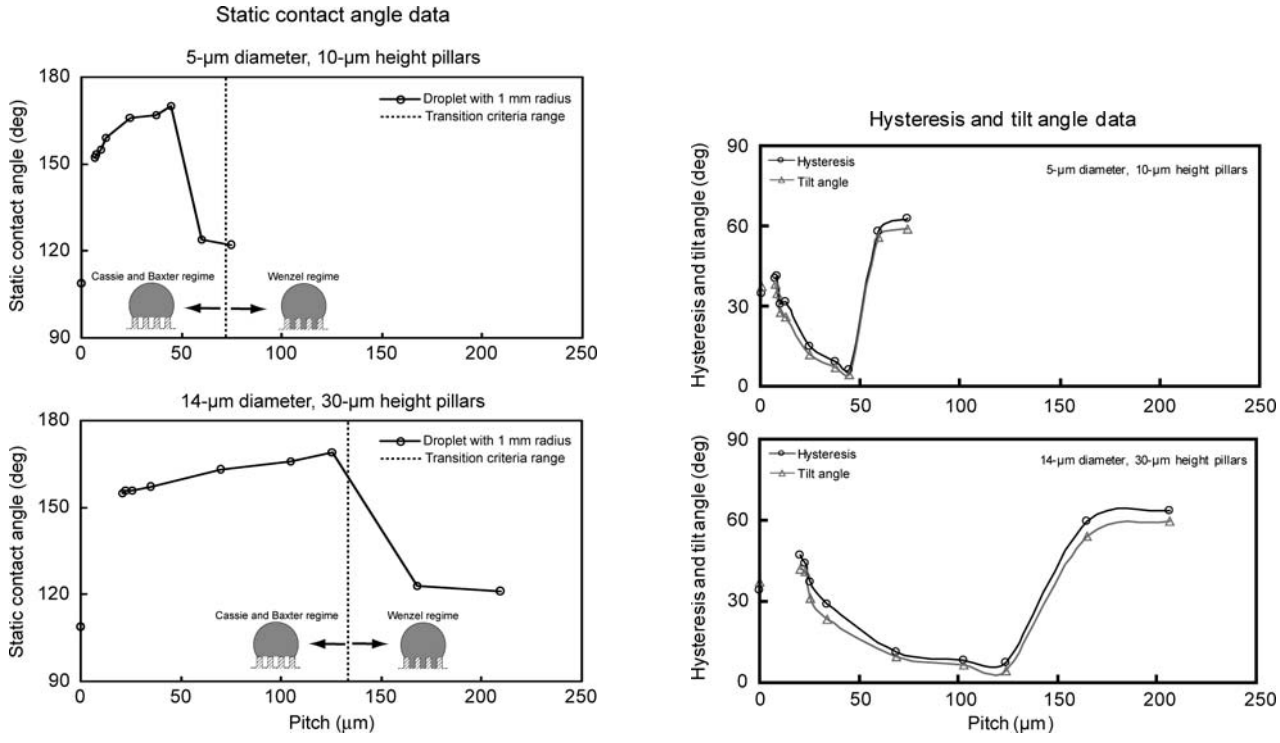

Fig. 11.8. a Static contact angle (a *dotted line* represents the transition criteria range obtained using (15)), and **b** hysteresis and tilt angles as a function of geometric parameters for two series of the patterned surfaces with different pitch values for a droplet with 1 mm in radius (5 μL volume). Data at zero pitch correspond to a flat sample [40, 173, 174]

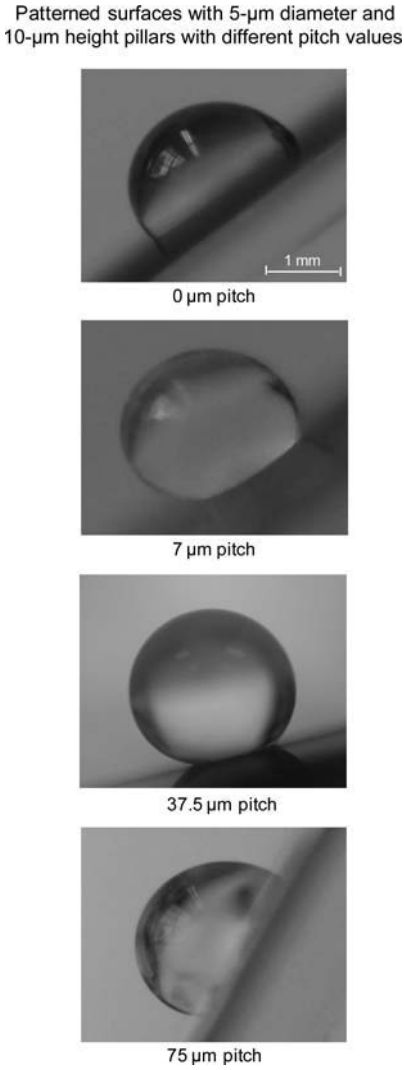

Fig. 11.9. Optical micrographs of droplets on the inclined patterned surfaces with different pitch values. The images were taken when the droplet started to move down. Data at zero pitch correspond to a flat sample [40]

hysteresis and tilt angles occurs due to the formation of composite interface at pitch values ranging from 7 μm to 45 μm in series 1 and from 21 μm to 126 μm in series 2. The hysteresis and tilt angles start to increase again due to the lack of formation of air pockets at pitch values raging from 60 μm to 75 μm in series 1 and from 168 μm to 210 μm in series 2. These results suggest that the air pocket formation and the reduction of pinning in the patterned surface play an important role for a surface with both low hysteresis and tilt angle [40]. Hence, to create superhydrophobic sur-

faces, it is important that they are able to form a stable composite interface with air pockets between the solid and the liquid. Capillary waves, nanodroplet condensation, hydrophilic spots due to chemical surface inhomogeneity, and liquid pressure can destroy the composite interface. Nosonovsky and Bhushan [244] suggested that these factors that make the composite interface unstable have different characteristic length scales, so nanostructures, or the combination of microstructures and nanostructures, is required to resist them.

11.3.2.4 Observation of the Transition during the Droplet Evaporation

Jung and Bhushan [173, 174] performed droplet evaporation experiments to observe the Cassie–Wenzel regime's transition on two different patterned Si surfaces coated with PF_3. The series of six images in Fig. 11.10 show the successive photos of a droplet evaporating on two patterned surfaces. The initial radius of the droplet is about 700 μm, and the time interval between successive photos is 30 s. In the first five photos, the drop is first in a hydrophobic state, and its size gradually decreases with time. However, as the radius of the droplet reaches 360 μm on the surface with 5-μm diameter, 10-μm height, and 37.5-μm pitch pillars, and 423 μm on the surface with 14-μm diameter, 30-μm height, and 105-μm pitch pillars, the Cassie–Wenzel regime's transition occurs, as indicated by the arrow. Figure 11.10 also shows a close-up of water droplets on two different patterned Si surfaces coated with PF_3 before and after the transition. The light passes below the left droplet, indicating that air pockets exist, so that the droplet is in the Cassie–Baxter state. However, an air pocket is not visible below the bottom right droplet, so it is in Wenzel state. This could result from an impalement of the droplet on the patterned surface, characterized by a smaller contact angle.

To find the contact angle before and after transition, the values of the contact angle are plotted against the theoretically predicted value, based on the Wenzel and Cassie–Baxter models. Figure 11.11 shows the static contact angle as a function of geometric parameters for the experimental contact angles before (circle) and after (triangle) the transition compared with the Wenzel and Cassie–Baxter equations (solid lines) with a given value of θ_0 for two series of the patterned Si with different pitch values coated with PF_3 [174]. The fit is good between the experimental data and the theoretically predicted values for the contact angles before and after transition.

To verify the validity of the transition criteria in terms of droplet size, the critical radius of the droplet deposited on the patterned Si with different pitch values coated with PF_3 was measured during the evaporation experiment. Figure 11.12 shows the radius of a droplet as a function of geometric parameters for the experimental results (circle) compared with the Cassie–Wenzel regime's transition (solid lines) for two series of the patterned Si with different pitch values coated with PF_3. It was found that the critical radius of impalement is indeed in good quantitative agreement with our predictions. The critical radius of the droplet increases linearly with the geometric parameter (pitch). For the surface with small pitch, the critical radius of a droplet can become quite small. Based on this trend, one can design superhydrophobic surfaces, even for small droplets.

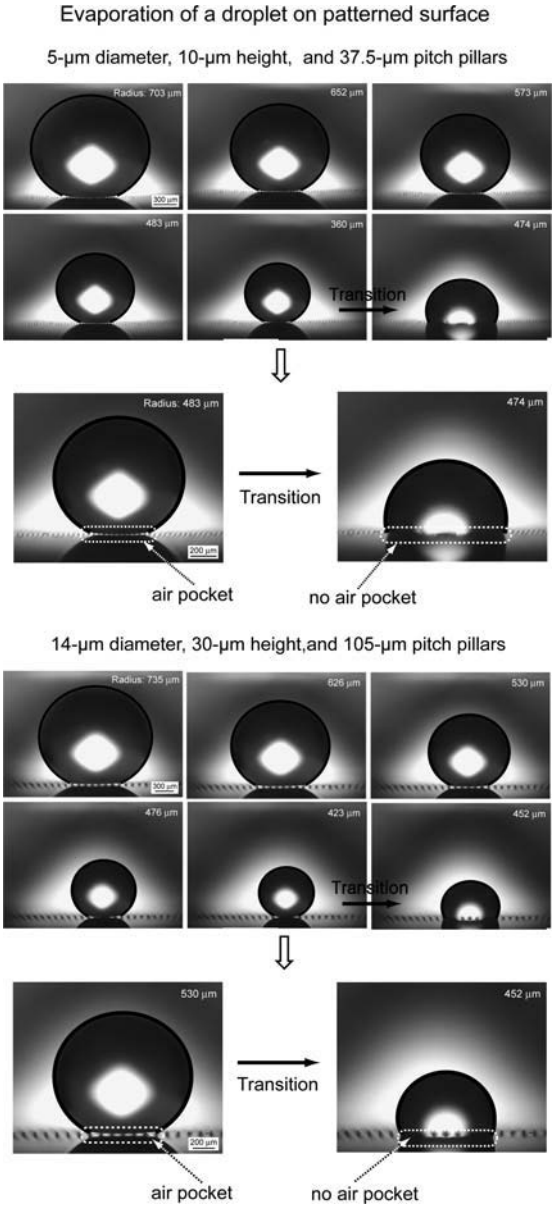

Fig. 11.10. Evaporation of a droplet on two different patterned surfaces. The initial radius of the droplet is about 700 μm, and the time interval between successive photos is 30 s. As the radius of droplet reaches 360 μm on the surface with 5-μm diameter, 10-μm height, and 37.5-μm pitch pillars, and 420 μm on the surface with 14-μm diameter, 30-μm height, and 105-μm pitch pillars, the transition from Cassie and Baxter regime to Wenzel regime occurs, as indicated by the arrow. Before the transition, air pocket is clearly visible at the bottom area of the droplet, but after the transition, air pocket is not found at the bottom area of the droplet [174]

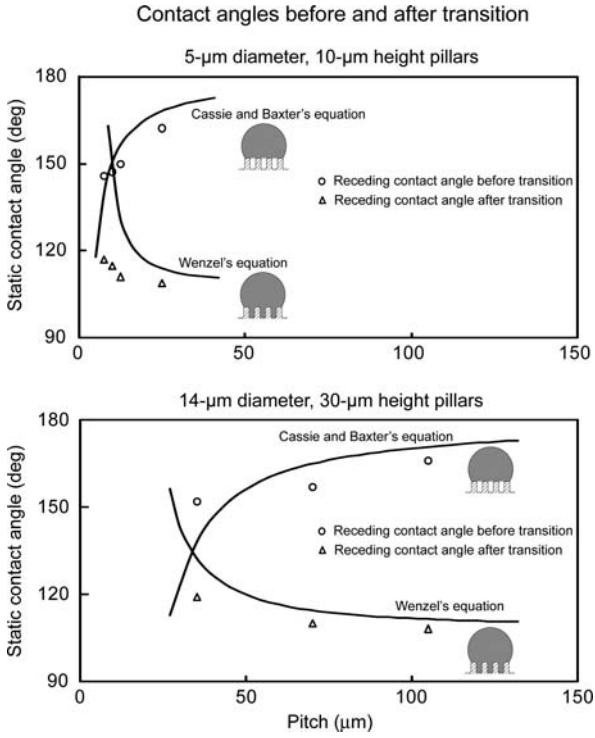

Fig. 11.11. Receding contact angle as a function of geometric parameters before (*circle*) and after (*triangle*) transition compared with predicted static contact angle values obtained using Wenzel and Cassie and Baxter equations (*solid lines*) with a given value of θ_0 for two series of the patterned surfaces with different pitch values [174]

To verify their transition criterion, Jung and Bhushan [173, 174] used another approach using the dust mixed in water. Figure 11.13 presents the dust trace remaining after droplet with 1 mm radius (5 μL volume) evaporation on the patterned Si surface with pillars of 5-μm diameter and 10-μm height with 37.5-μm pitch in which the transition occurred at 360 μm radius of the droplet, and with 7-μm pitch in which the transition occurred at about 20 μm radius of the droplet during the process of evaporation. As shown in the top image, after the Cassie–Wenzel regime's transition, the dust particles remained not only at the top of the pillars but also at the bottom with a footprint size of about 450 μm. However, as shown in the bottom image, the dust particles remained on only a few pillars until the end of the evaporation process. The transition occurred at about 20 μm radius of droplet and the dust particles left a footprint of about 25 μm. From Fig. 11.12, we observe that the transition occurs at about 300 μm radius of droplet on the 5-μm diameter and 10-μm height pillars with 37.5-μm pitch, but the transition does not occur on the patterned Si surface with pitch of less than about 5 μm. These experimental observations are consistent with model predictions. In the literature, it has been shown that on super-

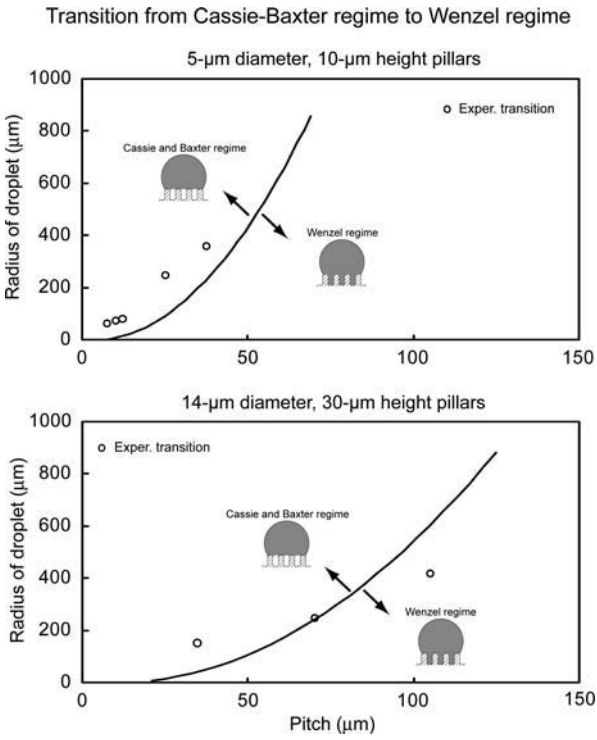

Fig. 11.12. Radius of droplet as a function of geometric parameters for the experimental results (*circle*) compared with the transition criteria from Cassie and Baxter regime to Wenzel regime (*solid lines*) for two series of the patterned surfaces with different pitch values [174]

hydrophobic natural lotus, the droplet remains almost in the Cassie–Baxter regime during the evaporation process [357]. This indicates that the distance between the pillars should be minimized enough to improve the ability of the droplet to resist sinking.

11.3.2.5 Observation and Measurement of Contact Angle Using ESEM

Figure 11.14 shows how water droplets grow and merge under ESEM [174]. ESEM is used as a contact angle analysis tool to investigate superhydrophobicity on the patterned surfaces. Microdroplets (in dimension of less than 1 mm diameter) are distributed on the patterned surface coated with PF_3 during increasing condensation by decreasing temperature. Even if the microdroplets are not the same size, they show the hydrophobic characteristics of the patterned surface. At the beginning, some small water droplets appear, i.e., water droplets at locations 1, 2, and 3 in the left image. During increasing condensation by decreasing temperature, water droplets at locations 1 and 3 gradually increase in size and water droplets at location 2 merge together to form one big droplet in the middle image. With further condensation, water

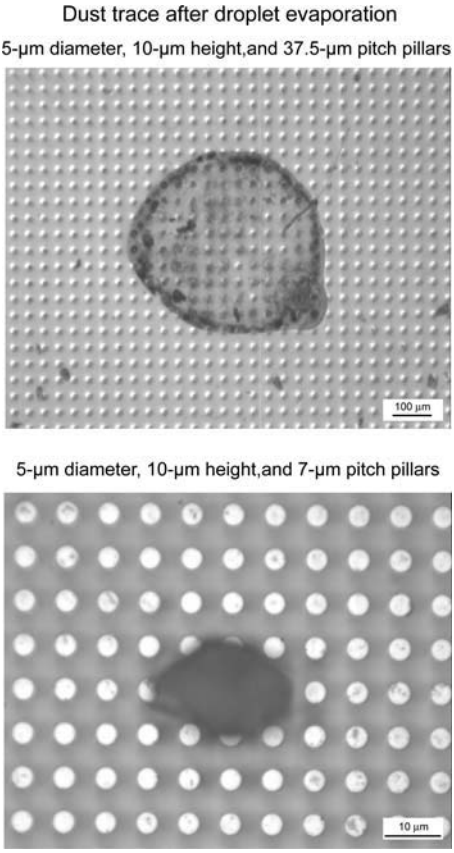

Fig. 11.13. Dust trace remained after droplet evaporation for the patterned surface. In the top image, the transition occurred at 360 μm radius of droplet, and in the bottom image, the transition occurred at about 20 μm radius of droplet during the process of droplet evaporation. The footprint size is about 450 and 25 μm for the top and bottom images, respectively [174]

droplets at locations 1 and 2 increase in size and water droplets at location 3 merge together to form one big droplet in the right image. In all cases condensation was initiated at the bottom, therefore, as can be observed, the droplets are in the Wenzel regime. This could also be evidence that the droplet on the macroscale used in the conventional contact angle measurement comes from the merging of smaller droplets [174].

Compared with the conventional contact angle measurement, ESEM is able to provide detailed information about the contact angle of microdroplets on patterned surfaces. The diameter of the water droplets used for the contact angle measurement is more than 10 μm such that the size limit pointed out by Stelmashenko et al. [303] was avoided. For droplet size less than 1 μm, substrate backscattering can distort the intensity profile such that the images are inaccurate [174].

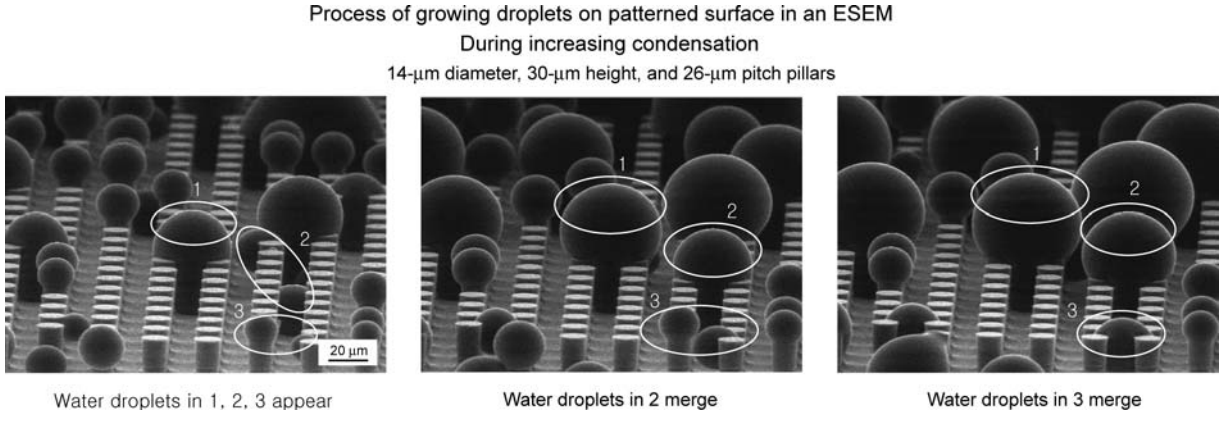

Fig. 11.14. Microdroplet (in dimension of less than 1 mm diameter) growing and merging process under ESEM during increasing condensation by decreasing temperature. *Left image*: Some small water droplets appear at the beginning, i.e. water droplets 1, 2, 3. *Middle image*: Water droplets at locations 1 and 3 increase in size and water droplets at location 2 merge together to form one big droplet. *Right image*: Water droplets at locations 1 and 2 increase in size and water droplets at location 3 merge together to form one big droplet [174]

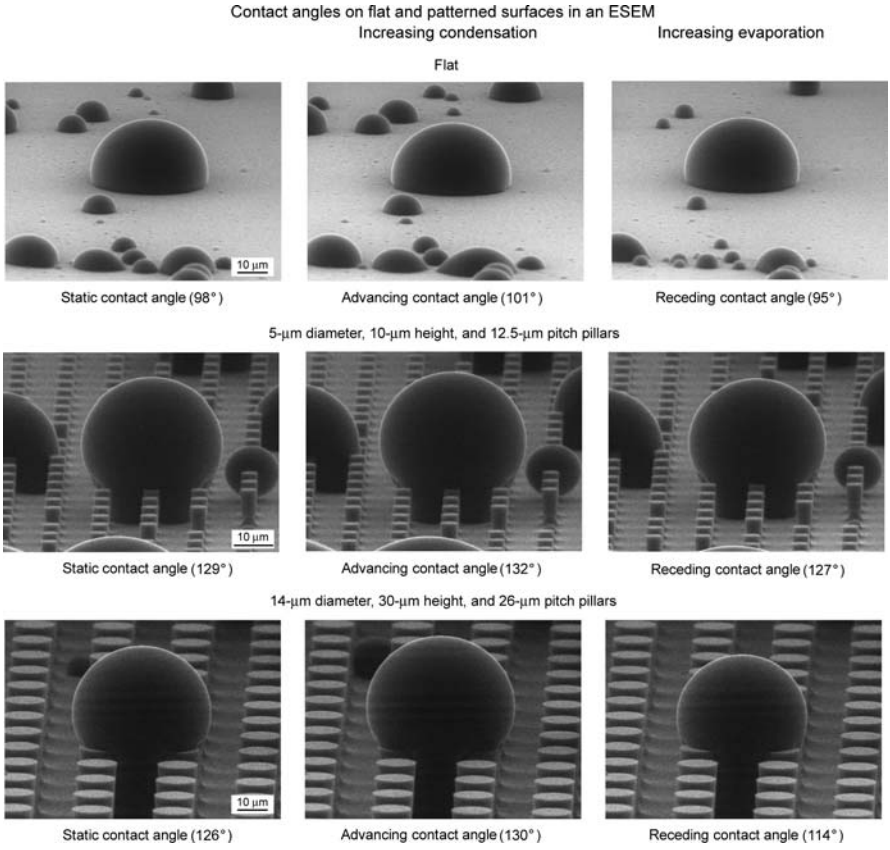

Fig. 11.15. Microdroplets on flat and two patterned surfaces using ESEM. Second set of images were taken during increasing condensation, and the third set of images were taken during increasing evaporation. Static contact angle was measured when the droplet was stable. Advancing contact angle was measured after increasing condensation by decreasing the temperature of the cooling stage. Receding contact angle was measured after decreasing evaporation by increasing the temperature of the cooling stage [174]

As shown in Fig. 11.15, the static contact angle and hysteresis angle of the microdroplets condensed on a flat surface and on two different patterned surfaces were obtained from the images and corrected using methodology mentioned earlier. The difference between the data estimated from the images and corrected θ is about 3%. Once the microdroplet's condensation and evaporation has reached a dynamic equilibrium, static contact angles are determined. The flat Si coated with PF_3 showed a static contact angle of 98°. The patterned surfaces coated with PF_3 increase the static contact angle compared to the flat surface coated with PF_3 due to the effect of roughness. The advancing contact angle was taken after increasing condensation by decreasing the temperature of the cooling stage. The receding contact angle was

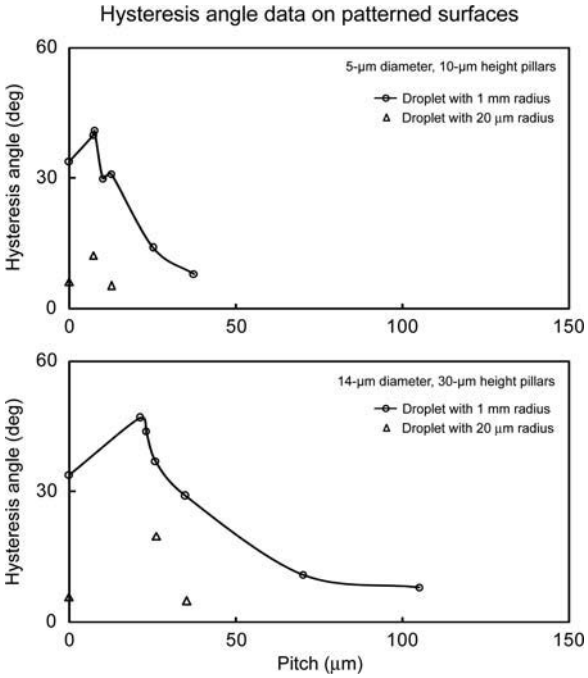

Fig. 11.16. Hysteresis angle as a function of geometric parameters for the microdroplet with about 20 μm radius from ESEM (triangle) compared with the droplet with 1 mm radius (5 μL volume) (circle and solid lines) for two series of the patterned surfaces with different pitch values. Data at zero pitch correspond to a flat sample [174]

taken after increasing evaporation by increasing the temperature of the cooling stage. The hysteresis angle was then calculated [174].

Figure 11.16 shows hysteresis angle as a function of geometric parameters for the microdroplets formed in the ESEM (triangle) for two series of the patterned Si with different pitch values coated with PF_3. Data at zero pitch correspond to a flat Si sample. The droplets with about 20 μm radii that are larger than the pitch were selected in order to look at the effect of pillars in contact with the droplet. These data were compared with conventional contact angle measurements obtained with the droplet with 1 mm radius (5 μL volume; circle and solid lines) [40]. When the distance between pillars increases above a certain value, the contact area between the patterned surface and the droplet decreases, resulting in the decrease of the hysteresis angle. Both the droplets with 1 mm and 20 μm radii show the same trend. The hysteresis angles for the patterned surfaces with low pitch are higher compared to the flat surface due to the effect of sharp edges on the pillars, resulting in pinning [240]. Hysteresis for a flat surface can arise from roughness and surface heterogeneity. For a droplet advancing on the patterned surfaces, the line of contact of the solid, liquid, and air will be pinned at the edge point until it is able to move, resulting in increasing hysteresis angle. The hysteresis angle for the microdroplet from ESEM is

lower compared to that for the droplet with 1 mm radius. The difference of hysteresis angle between a microdroplet and a droplet with 1 mm radius could come from the different pinning effects, because the latter has more sharp edges contacting with a droplet compared with the former. The results show how droplet size can affect the wetting properties of patterned Si surfaces [174].

11.4 Self-cleaning

Thus far there has been proposed no quantitative theory of self-cleaning that would relate, for example, the size and contact angle of a droplet with the size of a contaminating particle being washed away. There is a qualitative understanding that water-repellent surfaces do also repel other contaminants and that dust can easily be washed from them by flowing water. A number of experimental studies have been conducted. The self-cleaning abilities of patterned surfaces were investigated by Fürstner et al. [118]. They studied Si wafer specimens with regular patterns of spikes that were manufactured by X-ray lithography. The specimens were hydrophobized with Au thiol. For comparison, they also studied replicates of plant surfaces, made by a two-component silicon molding mass applied to the leaf surface. The negative replica is flexible and rubber-like. A melted hydrophobic polyether was applied onto this mold. They also studied several metal foil specimens, hydrophobized by means of a fluorinated agent. In order to investigate the self-cleaning effect, a luminescent and hydrophobic powder was used as a contaminant. Following contamination, the specimens were subjected to an artificial fog and rain [118].

Droplets of water rolled off easily from Si samples with a microstructure consisting of rather slender and sufficiently high spikes; this is attributed to the fact that the Cassie wetting state occurred. These samples could be cleaned almost completely after artificial contamination by means of the fog treatment. The behavior of water drops was different upon surfaces with low spikes and a rather high pitch. The researchers found a considerable decrease of the contact angles and a distinct rise in the sliding angles apparently corresponding to the Wenzel state. Some metal foils and some replicates had two levels of roughness. These specimens did not show a total removal of all contaminating particles when they were subjected to artificial fog, but water drops impinging with sufficient kinetic energy could clean them perfectly. A substrate without structures smaller than 5 μm could not be cleaned by means of fog consisting of water droplets with diameter 8–20 μm because this treatment resulted in a continuous water film on the samples. However, artificial rain removed all the contamination. On the other hand, smooth specimens made of the same material could not be cleaned completely by impinging droplets. This is a clear indication of the different contact phenomena on smooth hydrophobic surfaces in contrast to self-cleaning microstructured surfaces. Another interesting observation of this group was that despite the missing structure of the wax crystals, the water contact angle of the lotus replica was the highest of all the replicates, indicating that the microstructure formed by the papillae alone is already optimized with regard to water repellency [118].

11.5 Commercially Available Lotus-Effect Products

A number of products that use the lotus-effect are already commercially available or being developed. In addition, many patents have been granted for various possible applications of self-cleaning surfaces [45]. Most of these applications use the self-cleaning effect, especially in the case of glasses (for architecture, automotive, optical sensor, and other applications), roof tiles, and other architectural applications. Additionally, sprays and paints that create clean surfaces (e.g., graffiti-resistant) have been suggested, as well as water-repellent textiles. Some agricultural applications are also discussed (e.g., pesticide additives that can decrease bouncing off plant surfaces or increase penetration into the soil).

From a commercial point of view, cleaning of windows is expensive and cumbersome, especially if the windows are on a skyscraper. Self-cleaning windows using the Lotus-effect have been released to the market by several companies. How far these windows will be a commercial success remains to be seen [57]. The Germany-based Web site Lotus-Effekt.de, dedicated to the commercial application of patented self-cleaning superhydrophobic micro-to-nano structured surfaces, states the following:

"*Lotusan*®, an exterior paint from the firm *Sto* is marketed already with the greatest success since 1999. It is used by professional firms of house painters and is, not yet, available for the general building trade. Up to the present *Lotusan*® has been used to paint c. 300,000 buildings. In 2004 *Degussa* (daughter company of *Goldschmidt*) has introduced the first spray: *Tegotop*® 105 which can be used to impregnate surfaces. Self-cleaning textiles are being tested at present and will be available commercially from summer 2005. Marquees will probably the first to receive such treatment. Optical sensors in public high impact areas (for instance, toll bridge sensors on highways) are furnished already throughout Germany with Lotus-*Effect*® glass manufactured by *Ferro AG*. A series of further products is being tested, among these *Aeroxide*® LE of the *Degussa* for plastics. For years self-cleaning glasses have figured in advertisement. Frequently this is about so-called photo catalytic stratification. The firm *Ferro* keeps prototypes of architectural glass with Lotus-*Effect*® in permanent test conditions. In the region of optical sensors (toll bridges) Lotus-*Effect*® glasses are already used successfully. For architectural glass and rear windows of cars applications will probably follow soon. With *Erlus-Lotus*® the first self-cleaning roof in the world came on the market. For demonstrations we employ a spoon with a perfect Lotus-*Effect*® surface. Honey and many other substances roll off without a hint of residue. The spoon is a prototype that is, unfortunately, not for sale. Firms can already order the first spray Tegotop® 105 for testing from the *Degussa-Goldschmidt AG*. The properties of the new-fangled intelligent textiles are astonishing. Not only does water roll off, but ketchup and red wine do likewise. The area of use will hardly lie with suits, ties or shirts, but rather with outdoor clothing, marquees, tents and with tarpaulins for lorries" [10].

In addition to the household and "conventional" products, possible use of roughness- or heterogeneity-induced superhydrophobicity in nano- and biotechnology applications is often discussed. This includes, for example, nonsticky surfaces for the components of micro/nanoelectromechanical systems (NEMS/MEMS). Since adhe-

sion plays an important role for small devices, the so-called "stiction" of two component surfaces is a significant problem in that industry, which may lead to device failure. Making a surface hydrophobic can reduce meniscus force and stiction [249].

Controlling droplets containing biologically relevant molecules (DNA and proteins) is important in biotechnology. Superhydrophobicity is useful for these applications: the almost fully spherical droplets on a superhydrophobic surface can shrink exactly like a drop in free air. Furthermore, the positioning and shape of water droplets can be controlled by a pattern that combines hydrophilic and hydrophobic elements. Interestingly, some desert beetles capture their drinking water by a hydrophobic/philic structured back [259]. At a patterned heterogeneous substrate, hydrophilic regions can help to contain small liquid volumes of DNA, which may improve spotting and analyzing DNA and proteins by avoiding wall contact [57, 130].

In micro/nanofluidics, a guided motion of droplets on heterogeneous hydrophobic/philic surfaces gives the opportunity to develop droplet-based microfluidics systems, as opposed to the classical concept based on microfluidic channels. Droplets moving freely on open surfaces and bulk liquids flowing in channels constitute two extremes, with the patterned heterogeneous hydrophobic/philic surfaces being the intermediate between these two [102]. Driving the liquids along the channels and making them merge at predefined locations offers a novel way to mix reactants or steer biochemical reactions, defining the concept of a "liquid microchip" [128] or "surface-tension confined microfluidics" [199]. These open structures have advantages over capillaries, because blocking of the capillary by unforeseen chemical reactions cannot occur. Droplets have very low contact areas with the substrate, and they are easy to move by external fields, for example, electrostatic forces or surface capillary waves. Systems that make use of a droplet-based actuation mechanism are also being developed, and their aim is to control droplet positioning and motion on the substrates with as little surface contact as possible, and to turn the droplet-based system into a programmable reactor, by which the liquid positions are prescribed and tuned [57].

11.6 Summary

In this chapter, we discussed artificial superhydrophobic surfaces. There are several ways to manufacture these surfaces, and new methods continue to emerge. Some methods (such as lithography) allow scientists to create patterned surfaces with clearly defined and controlled geometrical features. These features have a typical size ranging from 1 μm to 100 μm. Other (and often cheaper) methods lead to self-assembled or random rough surfaces. This includes extending, etching, polymer solution evaporation, sol-gel, and other methods. There are technologies available to produce transparent superhydrophobic materials; hierarchical surfaces and switchable surfaces that can change from hydrophobic to hydrophilic under an external control. The difference in the superhydrophobic properties of surfaces with pattern and random structure still has to be investigated.

A proper control of roughness constitutes the main challenge to producing a reliable superhydrophobic surface, while if the initial material is hydrophilic, a surface treatment or coating is required that will decrease the surface energy. While the two factors—roughness and low surface energy—are required for superhydrophobicity, the role of roughness clearly dominates. For example, it is not really important whether the low energy surface is built of typical for paraffin $–CH_2–$ groups or having much lower energy $–CH_3–$ groups of fluorocarbons. Furthermore, many rough surfaces without any lower energy characteristics still exhibit superhydrophobicity. The role of hierarchical roughness still remains to be investigated. While many suggestions have been made regarding why superhydrophobic surfaces in nature are hierarchical, experiments with nonhierarchical patterned surfaces demonstrate superhydrophobicity as well.

In addition, we discussed a number of emerging applications of the lotus-effect, superhydrophobicity and controlled hydrophobicity, ranging from the household applications (glasses, paints) to nanotechnology and microfluidics.